Published in Physical Review B 69, issue 045312, 1-10, 2004
which should be used for any reference to this work

Electronic structure and Fermi surface of two-dimensional rare-earth silicides epitaxially grown on Si(111)

C. Rogero,[1] C. Koitzsch,[2] M. E. González,[1,3] P. Aebi,[2] J. Cerdá,[1] and J. A. Martín-Gago[1]
[1]*Instituto de Ciencia de Materiales de Madrid (CSIC), Cantoblanco, 28049 Madrid, Spain*
[2]*Institut de Physique, Université de Neuchâtel, CH-2000 Neuchatel, Switzerland*
[3]*Centro de Ciencias de la Materia Condensada, Universidad Nacional Autónoma de México, Ensenada, Baja California 22800, México*

The electronic structure and the Fermi surface of two-dimensional rare-earth silicides epitaxially grown on Si(111), YSi_2 and $GdSi_2$, have been studied by a combination of angle-resolved ultraviolet photoemission spectroscopy and density functional theory calculations. Both silicides present a very similar electronic structure, with two characteristic electronic bands below the Fermi energy. One crosses the Fermi energy near the $\bar{\Gamma}$ point of the surface Brillouin zone (hole pocket) and the other one close to the $\bar{M}$ point (electron pocket). These two bands arise from surface (localized) states and are responsible for all the Fermi surface features. The theoretical calculations are in good qualitative agreement with the experimental results, and also allow to examine the nature of the bonding between the rare earth and the neighboring silicon atoms. We have found a combination of sp metallic type bond together with covalent bonds involving the rare-earth *d* states and Si 3*p* states.

I. INTRODUCTION

During the last years a great effort has been made towards the understanding of the relationship between the electronic and atomic structure of two-dimensional (2D) systems. The aim behind these ideas is to control and tailor the electronic properties derived from the reduced dimensionality of a layer. Of a particular interest are the electronic bands close to the Fermi level as well as the Fermi surface, because of the large amount of processes in which they play a crucial role (transport, optical properties, magnetism, . . .). Experimental and theoretical surface sensitive techniques have to be used to gather information about these properties. In the last years angle-resolved ultraviolet photoemission spectroscopy (ARUPS) has proved to be a powerful tool to determine the Fermi surface and the occupied band structure of very thin films. Complementary, highly optimized density functional theory (DFT) based codes offer the possibility of finding the equilibrium geometry and examining its electronic structure.

Rare-earth (RE) silicides epitaxially grown on Si have been studied in detail because of their interesting technological applications, that could be derived from their low Schottky barrier height on *n*-type Si(111).[1–4] The bulk structure of the heavy RE silicides studied until now consists of a stack of alternating planes of RE and Si atoms. In the Si planes one atom out of six is missing, forming a $p(\sqrt{3}\times\sqrt{3})R30°$ superstructure, and leading to a $RESi_{1.7}$ stoichiometry.[5,6] Most of the RE silicides present a $p(1\times1)$ 2D phase at coverages of about 1 ML.[7–9] In contrast to the bulk, this phase does not include Si vacancies and therefore the film presents a $RESi_2$ stoichiometry. The atomic structure of the two-dimensional phase was first reported for $Si(111)+p(1\times1)$-$ErSi_2$,[10,11] and recently, the same model was proposed for other heavy RE silicides, such as Y, Dy, and Ho silicides[12–16] and germanides.[17] The geometry consists of an interfacial RE layer positioned at T_4 sites and with a Si bilayer on top. This top Si bilayer is rotated 180° about the surface normal with respect to the rest of bulk like Si(111) bilayers below the RE. The structure, typically denoted as B-T4, is sketched in Fig. 1.

The surface electronic band structure for these systems has only been studied for the $Si(111)+p(1\times1)$-$ErSi_2$.[11,18] ARUPS experiments show two bands crossing the Fermi level, originating 2D hole and electron pockets around the $\bar{\Gamma}$ and $\bar{M}$ points, respectively. These bands are responsible for

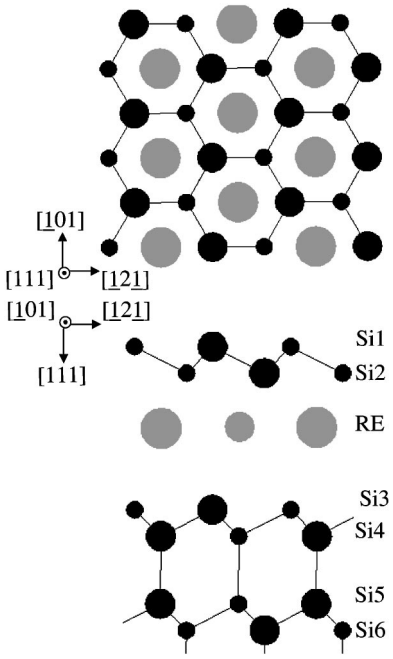

all the features appearing in the Fermi surface (FS).

The aim of this paper is precisely to provide a detailed electronic characterization for other Si(111)$+p(1\times1)$-$RESi_2$ systems, in order to generalize the previous results for Er to the rest of RE silicides that present a similar atomic structure. For this purpose, the Si(111)$+p(1\times1)$-YSi_2 and Si(111)$+p(1\times1)$-$GdSi_2$ surfaces were experimentally studied with ARUPS in order to determine their band structure and Fermi surface. The measured spectra are then compared against ARUPS simulations obtained from DFT based calculations within the local density approximation (LDA). Since the LDA fails to describe correctly the correlation effects associated to the highly localized *f* electrons, the theoretical study has been restricted to the YSi_2 system. Although Y has no *f* electrons, it is still considered a RE due to its trivalent nature. Moreover, and in order to ensure a meaningful experiment-theory comparison, we remove any finite size effects induced by the DFT slab geometry by transferring the DFT Hamiltonian to a semi-infinite model system which is solved via Green's functions matching techniques. Our approach allows one to identify any surface states, while the Green's functions formalism is better suited for incorporating certain aspects of the ARUPS experiment into the simulations.

The paper is organized as follows. In Sec. II we describe the experimental procedure, while Sec. III deals with the theoretical details. The experimental and theoretical results are shown and analyzed in Sec. IV. A brief discussion on these results is presented in Sec. V. Last, our conclusions are outlined in Sec. VI.

II. EXPERIMENTAL DETAILS

The experiments were performed in an ultrahigh vacuum chamber with a base pressure of 5×10^{-11} mbar. The photoemission spectra were recorded in a VG ESCALAB Mk II spectrometer with the sample mounted in a modified two-axis sample goniometer. Rotation is computer controlled for motorized angle-scanned data acquisition.[19,20] SiK_α was used for x-ray photoelectron spectroscopy in order to check the cleanness of the sample. Monochromatized He I and He II radiations (21.2 and 40.8 eV, respectively) from a discharge lamp were used for ultraviolet spectroscopy. The samples were kept at room temperature during the experiments. The ARUPS and the Fermi surface map measurements were performed using He I.

Full hemispherical FS maps (acquired over 2π solid angle) were constructed by sequential data acquisition of the total photoemission intensity at the Fermi energy for a complete range of polar and azimuthal angles. The angular resolution was 2° full cone and the energy resolution was set to 50 meV. The emission angles were transformed into $k_\parallel$ vectors.

ARUPS spectra are presented like dispersion maps as a function of specific $k_\parallel$ directions. The measurements were performed following the high symmetry directions of the surface Brillouin zone (SBZ), i.e., the $\overline{\Gamma}$-$\overline{M}$-$\overline{\Gamma}$ and $\overline{\Gamma}$-$\overline{K}$-$\overline{M}$ directions. For the results presented here the energy resolution was set to 30 meV and the polar angular resolution was 1°.

The YSi_2 and the $GdSi_2$ 2D silicides were prepared by depositing around 1 ML of RE on the 7×7 reconstructed substrate. The *n*-type Si(111) wafers were cleaned *in situ* by heating up to 1200 °C followed by slow cooling. The Y and Gd were deposited at RT and subsequently annealed at 400 °C for 15 min. The pressure during the evaporation was in the low 10^{-10} mbar. The formation of the 2D silicides was confirmed by the presence of a sharp 1×1 low energy electron diffraction pattern with traces neither the 7×7 nor $\sqrt{3}\times\sqrt{3}$ reconstructions (for more details see Ref. 15).

III. THEORETICAL DETAILS

The calculation of the structural and electronic properties of the Si(111)$+p(1\times1)$-YSi_2 was performed separately. We first determined the equilibrium geometry using the usual supercell approach where surfaces are modelled as thin slabs separated by vacuum.

However, for the electronic structure, it is desirable to avoid finite size effects associated with the slab geometry in order to unambiguously determine any 2D surface bands. To this end, we model the surface as a semi-infinite system and calculate its Green's function via standard matching techniques.[21,22] As will be shown below, the Hamiltonian for this system may still be calculated self-consistently with hardly any loss of accuracy as compared to the supercell approach.

Knowledge of the system's Green's function allows us to characterize the bonds at the surface, thus gaining further insight into the driving forces responsible for the B-T4 adsorption geometry. The main tools for this characterization are, apart from the usual charge density (CD) maps obtained from the slab calculations, the atomic orbital (AO) projected density of states (PDOS) and the crystal overlap populations (COOPs). Taking explicitly into account the overlap matrix *O*, the DOS projected at a given AO *i* and at energy *E*, may be written as:

$$\mathrm{PDOS}(E)_i=\frac{-i}{\pi}\sum_j O_{ij}G(E)_{ji}=\sum_j \mathrm{COOP}(E)_{ij},$$

where the summation over *j* includes all AOs that overlap with *i*, and $G(E)_{ji}$ is the Green's function matrix element linking AO *i* to AO *j*. The cross terms, $\mathrm{COOP}(E)_{ij}$, constitute a measure of the strength of the bond between the two AOs; the more positive (negative) the value of $\mathrm{COOP}(E)_{ij}$, the stronger the bonding (antibonding) character of the $i-j$ interaction.

The PDOS and COOP energy integrated counterparts are the Mulliken populations and the bond order (BO), respectively. Whereas the former gives the total charge associated to an AO or atom (ionic character), the latter provides the amount of charge shared between any two AOs or atoms.

A. Slab calculations

The slab calculations were performed with the SIESTA program.[23] This code uses the density-functional method and separable[24] norm-conserving Troullier-Martins[25] pseudopo-

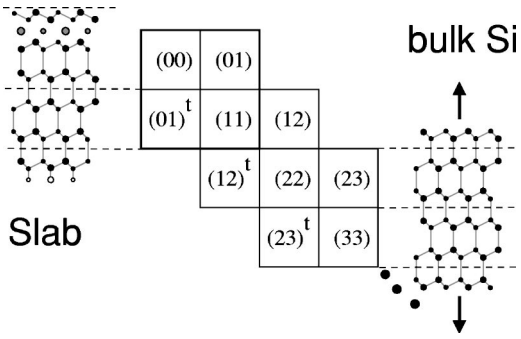

FIG. 2. The slab geometry for the atomic calculation is sketched at the left. Centered, scheme of the block tridigonal Hamiltonian matrix defined for the Si(111)$+p(1\times1)$-YSi_2 surface system. The matrix blocks for PLs 0 and 1 are extracted from the slab calculation. The rest of matrix blocks (Principal layers 2, 3, 4, etc.), are taken from the Si bulk calculation sketched on the right.

tentials. Valence wave functions are represented using pseudoatomic orbitals (PAOs),[26] including multiple-zeta and polarization functions.[27]

In all calculations we used the Ceperley-Alder[28] scheme for the LDA exchange-correlation functional. The pseudopotentials were expressly generated after relativistic atomic calculations, taking into account previous works.[5,15] For Si, we employed the usual $3s^2\ 3p^2$ configuration with a cutoff radius of $r_{cl}=1.89$ a.u. for all l values (beyond r_{cl} the pseudo-wave-functions match all the electron wave functions). For yttrium, we included the semicore $4p$ shell and used as atomic reference configuration $5s^1\ 4p^6\ 4d^2$, with $r_{cs}=2.96$ a.u., $r_{cp}=1.99$ a.u., and $r_{cd}=1.99$ a.u. The valence basis set consisted of double-zeta $3s$ and $3p$ and single-zeta $3d$ PAOs for Si, and double-zeta $5s$, $4p$, and $4d$ plus single-zeta $5p$ PAOs for Y. The pseudopotentials and the basis set were both carefully tested by performing structural and band calculations for bulk yttrium and bulk silicon. In particular, we obtained a lattice parameter for bulk Si of 3.84 Å and an energy gap of 0.54 eV.

The 2D SBZ was sampled using an 8×8 supercell. Other relevant parameters specific of SIESTA were set to the following values: a PAO energy shift of 50 meV and a mesh cutoff of 300 Ry. Whereas the former determines the real space extent of the PAOs, the latter sets the size of the grid employed for evaluating integrals in real space. We tested that the above values already yield converged results.

The complete slab geometry used in the calculation is sketched at the left of Fig. 2. The supercell contains six Si bilayers, one interfacial Y layer, and a H layer placed at the bottom of the slab in order to saturate the Si dangling bonds (monohydrated structure). We used the bulk Si lattice constant (3.84 Å) for the in-plane repeat vectors while the vacuum region was 10.6 Å thick. Test calculations including a further Si bilayer in the slab did not introduce any significant changes, signalling a good convergence on the slab thickness.

We used conjugate gradient dynamics for each trail structure, and let the system relax until the forces on all atoms were less than 0.04 eV/Å. All ions in the slab were allowed to relax except for the fourth and fifth bilayers, which were kept fixed in their bulk positions. In the final relaxed geometries, the residual forces on the fixed atoms were found to be small, confirming the validity of our slab modellization.

B. Surface calculations

In order to apply the DFT formalism to non-periodic systems such as a semi-infinite surface, we follow the same approach as the one used by Corbel *et al.* in the context of scanning tunneling microscopy simulations.[29] Similar techniques are becoming widely used for infinite systems which lack translational symmetry.[30] We first split the surface system into the so called principal layers (PLs). Each PL contains several atomic planes, and should be thick enough so that interactions between second nearest PL neighbors are already zero or negligible (i.e., only interactions between first nearest neighbor PLs are considered). Notice that this is always feasible and represents no approximation if one uses a linear combinations of atomic orbitals (LCAO) basis with strictly localized wave functions, such as the PAOs used by SIESTA. As shown in Fig 2, the Hamiltonian for such a system is a semi-infinite hermitian block tridigonal matrix, where each matrix block H_{ij} with $|i-j|\leqslant1$ holds the interactions between PLs i and j. The self-consistent elements in each matrix block are then obtained from separate SIESTA calculations, and the semi-infinite surface system is constructed by a sequential stacking of all these PLs.[21,22] The stacking process is carried out by solving the Dyson equation at each matching step.

In our case, the surface PL included the topmost rotated Si bilayer, the Y plane plus another two Si bilayers. The rest of PLs contained two bulk-like Si bilayers. If PLs are numbered from 0 to n as we move from the surface into the bulk, then the matrix blocks H_{00}, H_{01} and H_{11} may be directly extracted from the slab calculation described in the previous subsection. The rest of matrix blocks, H_{ii} and H_{ii+1}, with $i>1$, are then assumed to be bulklike (i.e., independent of i), and can be readily obtained from another SIESTA calculation performed just for bulk Si.

This approach would be exact if the surface effects were already fully screened at PL 1, in which case H_{11} would coincide with the diagonal bulk matrix block H^b_{ii}. Otherwise, the main approximation in the above procedure is the assumption that the Hamiltonian matrix elements in H_{11} do not change after replacing the adjacent H_{12} matrix block by the bulk one, H^b_{ii+1}. Care must be taken, however, to ensure that the matrix elements obtained from different SIESTA calculations are all referred with respect to the same energy origin. To this end, we have aligned the PDOS resulting solely from the H_{11} matrix block with the PDOS corresponding to the isolated bulk H^b_{ii} block (i.e., we consider in this test a 2D slab containing two Si bilayers). In Fig. 3(a) we show both PDOS curves; after the appropriate energy shift, they become indistinguishable in the graph, supporting the above *ansatz* of a bulklike behavior at PL 1. We have further checked the accuracy of our approach by computing the PDOS for an infinite stack of identical Si bulk PLs, but replacing only at a single PL the H^b_{ii} interaction by the slab-derived matrix block H_{11}, leaving the rest of PL interactions

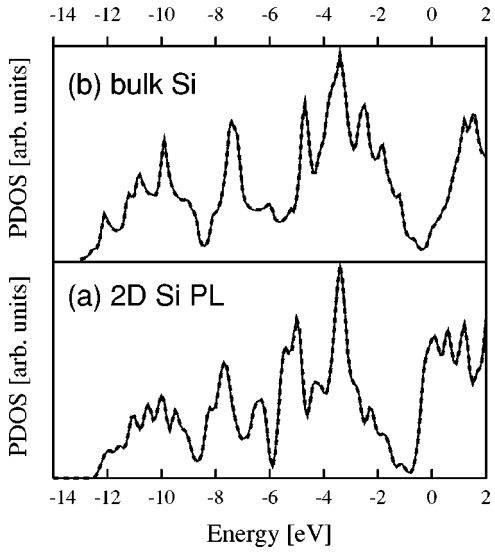

FIG. 3. PDOS projected onto a Si PL for (a) an isolated 2D slab and (b) bulk Si. Solid lines refer to a calculation where all Hamiltonian blocks are extracted from a Si bulk calculation, whereas for dashed lines the Hamiltonian diagonal matrix block at the projected PL is taken from the Si9 and Si10 atoms in the slab calculation.

to the bulk values. The comparison is shown in Fig. 3(b), and we again find an excellent agreement between the two.

For the PDOS and COOP calculations to be presented in Sec. IV, we employed a 21×21 supercell for the 2D Brillouin zone integration, while the imaginary part of the energy in the Green's function was set to 100 meV—recall that this value determines the width of the peaks in the PDOS(E) curves.

C. ARUPS Simulations

Despite the existence of elaborated theories for ARUPS simulations,[31–35] we employ a simplified approach which focuses on the initial electronic state, but that already allows one to rationalize most of the experimental ARUPS data measured for the YSi_2 system. A brief discussion on the validity of the approximations involved is given at the end of this subsection.

We consider a photon with energy $\hbar\omega$ exciting an electron in a state with a well defined energy E and $\vec{k}_\parallel$, while its perpendicular k-vector, $k_\perp$, before the excitation process, must satisfy the usual energy and momentum conservation relation:

$$k_\perp^{\hbar\omega}(E,\vec{k}_\parallel)=\sqrt{\frac{2m}{\hbar^2}(E+\hbar\omega+V_0)-|\vec{k}_\parallel|^2},$$

with V_0 giving the surface-vacuum potential step (typically between 5 and 10 eV).

The ARUPS arises both from surface (localized) states plus the states at PL 0 which couple to those bulk Bloch eigenvectors, $\vec{v}_B(k_\perp)$, with a perpendicular k vector $k_\perp$ close to $k_\perp^{\hbar\omega}$. An appropriate basis at the surface PL which allows one to discriminate both types of contributions may be readily obtained by performing a singular value decomposition[36] for the propagator $T_{0B}(E,\vec{k}_\parallel)$ linking the Bloch eigenvectors to the AOs at the surface. Dropping the E and $\vec{k}_\parallel$ for all matrices hereafter, T_{0B} may be obtained from

$$T_{0B}=G_{02}[G_{22}]^{-1}V_{2B},$$

where G_{ji} is the Green's function matrix linking PL i to PL j and, V_{2B} is the basis of the Bloch states projected at the bulklike PL 2. The SVD for this propagator then reads:

$$T_{0B}\ \ U_B=U_0\ \ \Sigma_{0B},$$

where U_0 and U_B are orthonormal basis for the surface PL and the Bloch eigenstates, respectively, and Σ_{0B} is a rectangular diagonal matrix holding the singular values. U_0 may be split into two orthogonal subspaces: $U_0=U_0^{ss}\otimes U_{0B}$. U_0^{ss} consists of those vectors in U_0 which have a null singular value and, hence, do not couple to the bulk (surface states). On the contrary, U_{0B} contains the vectors with nonzero Σ_{0B} elements, and spans the subspace at the surface PL which is linked to the bulk eigenvectors.

Next, the $k_\perp$ filtering may be accomplished by transforming the U_{0B} basis into a $k_\perp^{\hbar\omega}$ dependent one:

$$U_{0B}^{\hbar\omega}=F^{\hbar\omega}\ \ U_{0B},$$

where we have introduced the real diagonal $F^{\hbar\omega}$ matrix that weights each element in U_{0B} associated to a Bloch eigenstate $\vec{v}_B(k_\perp)$ by the factor $\sqrt{f(|k_\perp^{\hbar\omega}-k_\perp|)\cdot w^{\hbar\omega})}$. Here, f is a delta type function centered at $k_\perp^{\hbar\omega}$, and with a $w^{\hbar\omega}$ inverse width.

Combining the $U_{0B}^{\hbar\omega}$ and U_0^{ss} basis, we obtain the ARUPS transformation matrix: $U_0^{\hbar\omega}=U_0^{ss}\otimes U_{0B}^{\hbar\omega}$, which may be applied to the surface projected DOS matrix, ρ_0:

$$\rho_0^{\hbar\omega}=[U_0^{\hbar\omega}]^\dagger\rho_0\ U_0^{\hbar\omega}.$$

Here, $\rho_0=(i/\pi)(G_{00}-G_{00}^\dagger)$ is obtained from the Green's functions of the surface system following the procedure outlined in the previous subsection.

The ARUPS yield, $I^{\hbar\omega}(E,\vec{k}_\parallel)$, is then taken proportional to a weighted trace of $\rho_0^{\hbar\omega}$, via

$$I^{\hbar\omega}(E,\vec{k}_\parallel)\propto Tr[\Lambda\ \ \rho_0^{\hbar\omega}(E,\vec{k}_\parallel)],$$

where Λ is a real diagonal matrix giving the attenuation factor for each AO i contained in the surface PL: $\Lambda_i=e^{-z_i/\lambda}$, z_i being the normal distance between AO i and the surfacemost atom and λ the attenuation constant accounting for the reduction in the photo-electron flux due to inelastic processes (i.e., the deeper the AO into the bulk, the stronger the attenuation).

For our simulations, we set $\lambda=6$ Å, and $V=7$ eV, and for the broadening function $f^{\hbar\omega}(k_\perp)$ we employed a Lorentzian function with an inverse width $w^{\hbar\omega}=2$ Å. We checked that varying the above values within reasonable limits had hardly any effect on the simulations.

Fermi surfaces are then obtained after plotting the $I^{\hbar\omega}(E,\vec{k}_\parallel)$ quantities integrated over a ±100 meV energy interval around the Fermi level and weighted by the Fermi-

Dirac distribution ($kT=20$ meV). The surface bands dispersions are also plotted in an analogous way to the experimental data; $I^{\hbar\omega}(E,\vec{k}_{\parallel})$ is represented as a gray scale 2D map for $\vec{k}_{\parallel}$ along high symmetry reciprocal space directions. The imaginary part of the energy entering the Green's functions was set to 20 meV for the surface band dispersion plots, and to 50 meV for the FS maps. Finally, the theoretical Fermi level was fixed to that obtained from the slab calculation. Our approach omits several important processes related to the ARUPS experiment and which we briefly discuss below.

(i) The photoelectron intensity is modulated by the photon-electron matrix elements, which may affect the relative weights of each atomic PDOS or, more precisely, each *lm* component.[37] Although for non-polarized photons, as it is the current experimental case, this effect is reduced, it may still be quite relevant. Furthermore, interference effects between the photoelectron amplitudes arising from different atoms in the unit cell may also modify the aspect of the FS.[38]

(ii) Photoelectrons are excited with kinetic energies of a few tens of eV. In this regime, the multiple scattering events that the electron suffers before exiting the system are not negligible, introducing a further dependence of the total ARUPS yield on the energy of the emitted electrons and their direction upon exit, that is, $\vec{k}_{\parallel}$. In general, multiple scattering effects should not introduce important changes in the ARUPS dispersion plots, whereas for FSs, it may turn lighter or darker specific features.

(iii) DFT-LDA is well known to introduce sensible errors in the energy positions of the electronic bands. This limitation does not only apply to the excited states, since GW-corrected spectra for different systems have also shown large self-energy corrections for valence (occupied) states, particularly when they present a strong localization.[39,40] Furthermore, after the photoelectron excitation process, the electron has to surpass the attractive interaction with the hole just created before exiting, leading to a further renormalization of the energy bands. Although for metallic systems the magnitude of the LDA errors tends to be small, in semiconductors and insulators it may vary from a few hundredths of eV up to more than 1 eV. In any case, the theory-experiment surface bands comparisons presented in the next section will actually determine what is the DFT-LDA error in this sense.

IV. RESULTS

A. Atomic structure

Aside from the B-T4 structure already described in the introduction and sketched in Fig 1, we also tested a T4 structure, similar to the B-T4, but without the rotation of the top Si bilayer with respect to the Si bulklike bilayers. After the energy minimizations explained in the previous section, we have found the B-T4 geometry to be more stable than the T4 by 238 meV, in agreement with the experimental findings.[15] In the final geometry, there are no relevant inplane atomic displacements, so that the slab preserves the $p3m$ ($c3vm$) symmetry proper of the B-T4 model. The relaxed atomic positions are quite similar to those derived from a LEED analysis for the same surface. The corresponding comparison is shown in Table I, together with other theoretical results. The largest discrepancy corresponds to the Y-Si3 interlayer spacing, for which the SIESTA value is 0.09 Å smaller than the LEED value. The generalized gradient approximation derived structure does not present a better overall agreement, since although the Y-Si3 distance is better reproduced, the Si2-Y interlayer spacing becomes 0.08 Å smaller than the LEED result.

TABLE I. Interplanar distances between atomic planes (in Å) along the (111) direction, obtained from our SIESTA slab calculations for the YSi2/Si(111)-(1×1) system. They are compared against the LEED derived structure and the *ab initio* calculations of Ref. 15

Atoms	LEED	DFT-LDA (SIESTA)	DFT-GGA (VASP)
Si1-Si2	0.79	0.84	0.79
Si2-Y	1.85	1.83	1.77
Y-Si3	2.08	1.99	2.05
Si3-Si4	0.90	0.92	0.90
Si4-Si5	2.35	2.35	-
Si5-Si6	0.78	0.77	-

All Si-Si nearest neighbor distances attain values close to the bulk, $d_{Si-Si}=2.35$ Å, except for the second bilayer, where a significant expansion of the bilayer thickness from 0.78 Å to 0.92 Å, leads to a slightly elongated Si-Si bond length of $d_{Si3-Si4}=2.40$ Å. On the other hand, following the notation of Fig. 1, the Y bonding configuration presents a marked asymmetry, as it makes three short bonds ($d_{Y-Si2}=2.9$ Å) and three long bonds ($d_{Y-Si1}=3.5$ Å) with the Si atoms at the top bilayer, while for the bilayer below, there is one short bond ($d_{Y-Si4}=2.9$ Å) and another three slightly longer ($d_{Y-Si3}=3.0$ Å).

B. Bond analysis

In Fig. 4 we first present the CD maps for a plane perpendicular to the $[\bar{1}01]$ direction. This plane contains both the Y and Si atoms and it corresponds to the side view of Fig 1. The plot at the top of the figure shows the total valence CD, with darker regions corresponding to larger CD values. Notice that the contribution from the Y $4p$ semicore shell has been substracted out. The covalent nature of the Si-Si bonds is immediately apparent from the highly localized regions of charge pile up linking the Si atoms. On the other hand, the CD around the yttrium ion is spherical, suggesting a metallic character for this ion.

A better insight to the nature of the Y-Si bond is obtained after inspecting the CD difference (CDD) between the total valence CD and a superposition of the individual atomic CDs, displayed at the bottom of the figure. Positive (darker) CDD elongated regions link the Y to the dangling bonds of the upper and lower Si ions in the bilayer on top of and below the Y, Si2, and Si3, respectively, indicating certain amount of covalent bonding. The remaining closed regions of positive CDD arise from out of plane Si atoms. Surprisingly, there is no apparent bonding between the Y and the

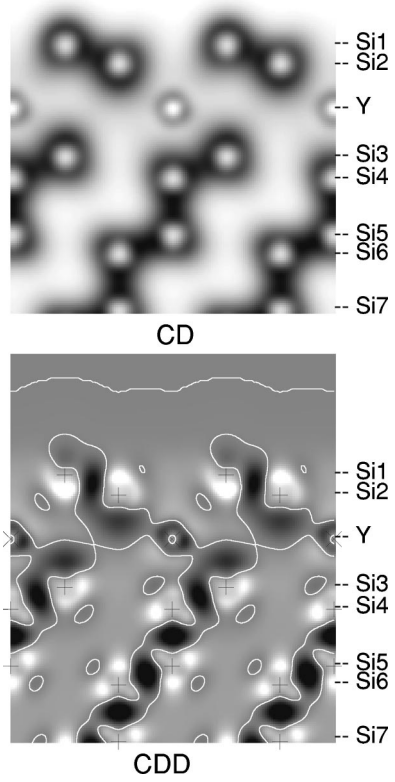

FIG. 4. Charge density (CD) and CD difference (CDD) plots for the YSi_2 slab along a plane perpendicular to $[\bar{1}01]$ direction and containing both Y ($\times$) and Si ($+$) atoms. In the CDD plot, the contour lines separate positive (darker) CDD regions from negative (lighter) regions. For the CD plot, darker regions correspond to larger CD values.

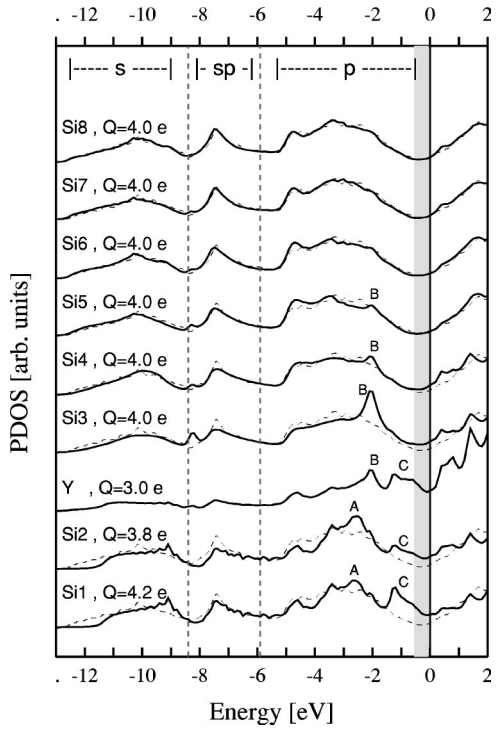

FIG. 5. DOS(E) projected on the first nine atoms of the YSi_2 surface (semi-infinite) system. The atomic Mulliken charges, Q, are also given. In all Si projections, the dashed curves correspond to the bulk Si PDOS. The energy origin is at the Fermi level. The Si band gap is indicated by the gray vertical stripe, while the dashed vertical lines roughly delimit the energy regions for the *s*, $s-p$, and *p* bands in bulk Si.

lower Si at the bilayer below, Si4, despite their small interatomic distance, $d_{Y-Si4}=2.9$ Å.

The DOS projected on the first nine atoms of the slab is displayed in Fig. 5. In each Si curve, the DOS projected at a bulk Si atom is also presented for comparison (dashed lines). Significant changes in the electronic structure with respect to the bulk are only seen for the first four Si atoms. The surface has a 2D metallic character, since the PDOS for the surface-most atoms experiences a considerable increase around the energy gap but becomes already bulk-like at the Si5. In the top bilayer both Si atoms (Si1 and Si2) present very similar PDOS. This is actually not surprising after noting the similarities between the CD around both ions in Fig. 4. The bandwidth of their lowest energy states (s bands) are slightly contracted, while the *p* bands centered at around -2.7 eV (label *A* in the figure) become more prominent. These features are a consequence of the fact that both ions lose a covalent bond each, leading to more localized states (less dispersive bands). Also, new occupied states appear close to the Fermi level, labeled in the graph as *C*. In this energy region, the peaks are clearly more pronounced for Si1, and have mainly p_z character while, for Si2, the p_z contribution drastically drops and becomes comparable to the *d* contributions.

The electronic structure of the Si3 resembles more that of the Si bulk atoms than those at the top bilayer. Apart from a new peak located at -8.2 eV, the most relevant feature is the large peak at -2.0 eV (*B* in the figure) with a major p_z contribution. This state extends into the bulk down to the next bilayer, as the peak can still be resolved in the Si5 spectra.

The Mulliken population analysis given in Fig. 5 only shows certain charge transfer (~ 0.2) from the Si2 to the Si1. Most of the charge difference between the two is localized in energy close the Fermi level (*C* states). The rest of the atoms remain essentially neutral, indicating that the Y-Si bonding has hardly any ionic character.

The local density of states corresponding to the *A*, *B*, and *C* energy regions is displayed in Fig 6. The plots reveal that each set of peaks is associated with the Si2, Si3, and Si1 dangling bonds, respectively. In all cases, certain charge pile

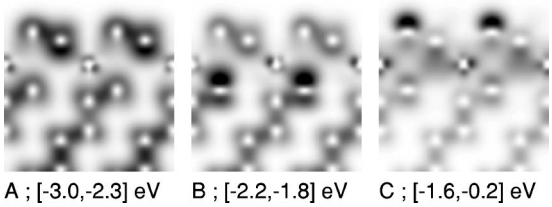

FIG. 6. CD plots for the same plane as in Fig. 4, corresponding to the local density of states (LDOS) centered at peaks *A*, *B*, and *C* and integrated over the energy ranges indicated at the bottom of each plot. Darker regions correspond to larger CD values.

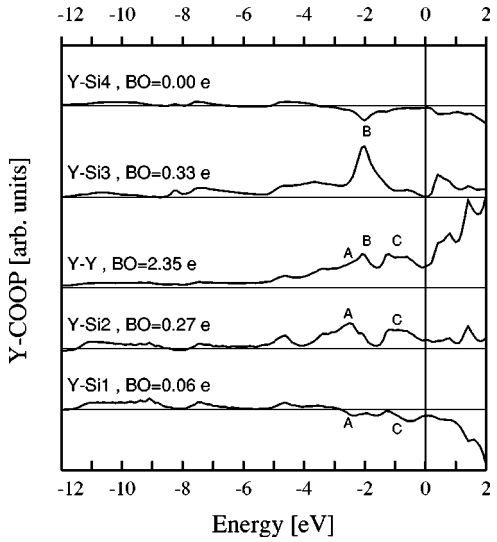

FIG. 7. COOP(E) plots between the Y atom and the first five atoms of the YSi_2 surface (semi-infinite) system. All Si-Y plots have been rescaled by a factor of 5. The gray horizontal lines in each plot give the COOP=0 level. The BO value for each interaction is also given.

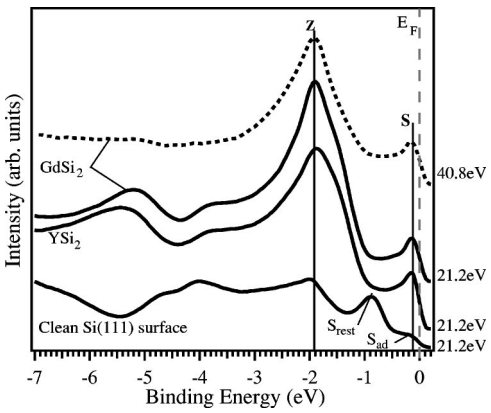

FIG. 8. Normal emission UPS spectra of the Si(111)$+p(7\times7)$ (at the bottom), YSi_2 and $GdSi_2$ measured using He I and He II radiation.

up with d symmetry can be observed at the Y atoms, always pointing away from the Y-Si dangling bond direction.

By noticing that the *A*, *B*, and *C* related peaks are also present in the Y PDOS, it seems clear that they involve Y-Si bonds. This is confirmed after inspecting the energy resolved COOPs relevant to the Y, which are given in Fig. 7. A common feature to all the Y interactions is that the lower energy part in the graphs present positive COOPs arising from the metallic bonding between the Si *s* and *p* states with the highly dispersive Y *s* and *p* bands. The Y *d* states appear at around -5 eV, and they dominate the COOPs above this energy. Curiously, they form bonding states with the Si2 and Si3 *p* bands, but show antibonding regions with the Si1 and Si4. An inspection to the BO values quoted in the figure shows that the Y-Si3 constitutes the strongest RESi bond. The BOs for the Si1 and Si2 are both smaller, although their sum is roughly equal to the BO(Y-Si3) value.

The prominent *B* peak at -2.0 eV is clearly identified in the COOPs, confirming the covalent type bond between the Si3 p_z AO and the Y *d* states already apparent in Fig. 6*B*. In the Y-Si2 COOPs, on the other hand, both the *A* and *C* peaks are present with similar heights, despite the fact they are mainly localized at the Si2 and Si1, respectively.

In summary, the RE forms an *sp* metallic type bond with its first four neighbor Si atoms (Si1-Si4), together with more covalent type bonds between the RE d states and the Si1, Si2 and Si3 dangling bonds.

C. Surface bands

Figure 8 shows valence band photoemission spectra recorded in normal emission for the 2D Si(111)$+p(1\times1)$-YSi_2 and Si(111)$+p(1\times1)$-$GdSi_2$ surfaces and for the clean Si(111)$+p(7\times7)$ surface. The spectrum from the reconstructed substrate shows the well known surface features, S_{ad} and S_{rest}, which have been ascribed to the adatoms and restatoms dangling bonds, respectively.[41,42] The state S_{ad} appears at -0.2 eV of binding energy, and its inherent width is responsible for the emission at energies close to the Fermi energy. The state S_{rest} appears at -0.8 eV, in good agreement with previous works.[41,42]

It is clear from the figure that the formation of the 2D silicide originates an increase of the number of counts at the Fermi edge, indicating the metallic character of the layer, in accordance with the theoretical findings. The YSi_2 and $GdSi_2$ spectra are both very similar, showing two well resolved peaks specific of the silicide (labeled *S* and *Z* in the figure), at binding energies of -0.1 and -1.9 eV, respectively. The upper spectra (dotted line) has been measured with a photon energy of 40.8 eV. Since the *Z* and *S* peaks do not shift in binding energy when the photon energy is varied, they do not disperse with $k_\perp$ and, therefore, they can be ascribed to surface states.

The left part of Fig. 9 shows bidimensional representations of the experimental ARUPS yield dispersion as a function of $\vec{k}_\parallel$ for the 2D Si(111)$+p(1\times1)$-YSi_2 along the $\bar{\Gamma}$-$\bar{M}$-$\bar{\Gamma}$ and $\bar{\Gamma}$-$\bar{K}$-$\bar{M}$ directions. In the images, darkest (brightest) features correspond to more (less) intense photoemission peaks. Same type of surface bands were recorded for $GdSi_2$ (right part of Fig. 9) Along $\bar{\Gamma}$-$\bar{M}$-$\bar{\Gamma}$ (bottom left in the figure), a parabolic surface band can be clearly observed. Experimentally, the bottom of this band appears at the $\bar{M}$ point of the SBZ, with a binding energy of -1.6 eV. This band crosses the Fermi edge close to the $\bar{\Gamma}$ point, at $k_F = 0.1$ Å^{-1}, leading to the formation of a hole pocket, similar to the one reported for $ErSi_2$.[18] Around the $\bar{M}$ point, and close to the Fermi energy, an increase of the photoemission intensity can be seen. Again, in analogy to the $ErSi_2$ case, one may *a priori* assign this feature to an electron pocket with a $k_F = 0.7$ Å^{-1}. Similar features are observed in the ARUPS dispersion curves for the $\bar{\Gamma}$-$\bar{K}$-$\bar{M}$ direction (top left of Fig. 9). The hole and electron pockets at $\bar{\Gamma}$ and $\bar{M}$ are again clearly visible, with $k_F = 0.1$ Å^{-1} and $k_F = 1.4$ Å^{-1}, respectively.

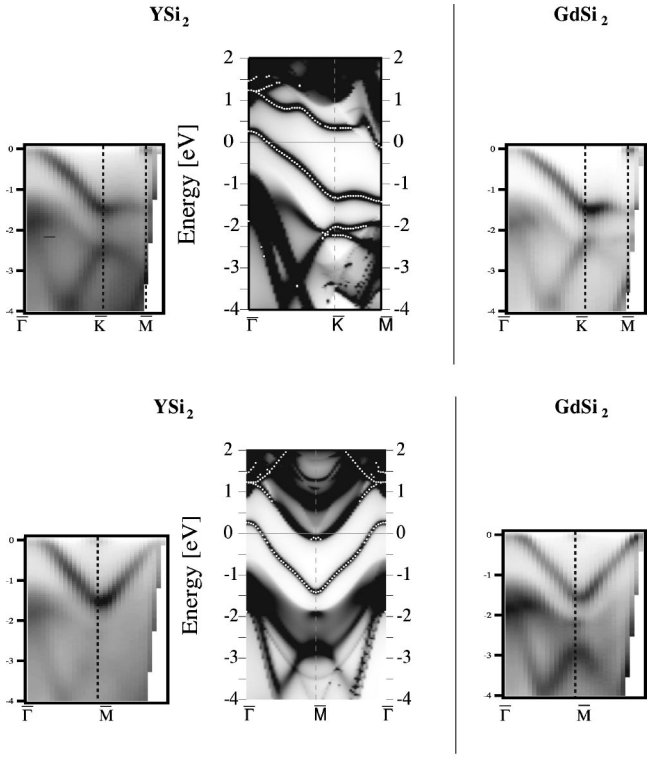

FIG. 9. Surface band dispersions along the $\bar{\Gamma}$-$\bar{K}$-$\bar{M}$ (top plots) and $\bar{\Gamma}$-$\bar{M}$-$\bar{\Gamma}$ (bottom plots). Plots at the left (center) correspond to the experimental (theoretical) ARUPS data for YSi_2. Results from $GdSi_2$ are shown at the right. Darker regions correspond to larger ARUPS yields. In the theoretical plots, surface states are indicated by small white circles. See text for further details.

Next to each experimental plot for the YSi_2, we also represent the associated theoretical ARUPS simulations, $I^{\hbar\omega}(E,\vec{k}_{\parallel})$, obtained as explained in Sec. III C. The surface states are also indicated in this plot by small circles overimposed to the ARUPS yields. The theoretical plots are in nice qualitative agreement with the experimental data despite all the approximations involved. The bottom of the hole (electron) pocket band is located at -1.4 eV (-0.1 eV).

The hole pocket band remains a surface (localized) band throughout its entire energy dispersion range for both directions. An AO decomposition for this band reveals that, at the bottom ($\bar{M}$ point), the main contributions arise from the Y-*d* and -*s* states, together with the Si1-p_z, although contributions from the Si2 and Si3 p_x and p_y AOs are not negligible. The Si1-p_z component increases at $\bar{K}$ becoming predominant, while at the top of the band ($\bar{\Gamma}$), the states are essentially a mixture of Y-d_{z^2} and Si3-p_z. Obviously, the lower part of this band is responsible for the *C* peaks discussed in the previous subsection.

As for the electron pocket band, we only find surface (localized) states in the flat region at the bottom of the band, ($\bar{M}$ point), which is precisely where no bulk states are available. The Si2-*p* AOs (mainly the p_z component) together with the Y-*s* and -d_{z^2} AOs yield the largest contributions.

There also exist two bands containing surface states around $\bar{K}$ at ~ -2 eV. They both have large Y-*d* components, together with Si2-p_z (Si3-p_z) components for the upper (lower) energy bands. The former is responsible for peak *B*, whereas the latter gives the off-set for the set of peaks *A*.

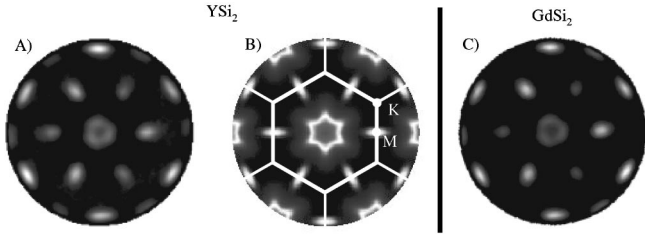

FIG. 10. (A) Experimental and (B) theoretical Fermi surface maps for Si(111)+$p(1\times1)$-YSi_2 system. (C) Experimental Fermi surface map for the Si(111)+$p(1\times1)$-$GdSi_2$.

Figures 10(A) and 10(B) show the experimental and theoretical FS maps obtained for Si(111)+$p(1\times1)$-YSi_2, with the SBZ drawn overimposed in the theoretical plot (B). At a photon energy $\hbar\omega=21.2$ eV, we have only access to the first SBZ and a small part of the next ones. In this case, lighter regions in the pattern correspond to higher photoemission intensities and, therefore, to the presence of electronic states. All the experimental features are reproduced by the theory, although there exist qualitative differences in their shape that will be discussed in the next section. In Fig. 10(C) we also present the FS for the $GdSi_2$ system, which is again very similar to the YSi_2 map. They both present a ring centered at $\bar{\Gamma}$ and ellipses at $\bar{M}$ with their long axis aligned along the $\bar{\Gamma}$-$\bar{M}$ direction. Their origin is easily understood after the above surface band dispersion analysis. The hole pocket band crosses the Fermi level close to $\bar{\Gamma}$ both along the $\bar{\Gamma}$-$\bar{M}$ and $\bar{\Gamma}$-$\bar{K}$ directions (see Fig. 9), leading to the ring structure. The electron pocket band, on the other hand, has its minimum at $\bar{M}$, and presents a larger dispersion along $\bar{M}$-$\bar{K}$ than along $\bar{M}$-$\bar{\Gamma}$, thus generating the elliptical features.

It is important to recall that the states contributing to the FS shape are essentially surface states (see Fig. 9). Therefore, the features shown in the FS should not depend on the experimental photon energy, as it has been reported for $ErSi_2$.[43]

V. DISCUSSION

Let us first discuss on the overall experiment-theory agreement for the ARUPS spectra shown in Fig. 9. Although all experimental features are well reproduced by the theory, there are sensible deviations in the energy location of the bands. The bottom (top) of the hole pocket band at $\bar{M}$ ($\bar{\Gamma}$) is located at -1.40 eV (0.26 eV) in the theoretical plots, whereas the corresponding experimental value is -1.6 eV (~ 0.1 eV). As for the electron pocket band, both spectra show the band minimum just below the Fermi level, at ~ -0.1 eV. The identification of the predicted surface states around $\bar{K}$ at ~ -2 eV is not so clear in the experimental plots, although similar features to the theoretical ones can be seen at about -2.3 eV. We may conclude that DFT-LDA introduces errors of the order of 200–500 meV for localized

(occupied) states. As pointed out earlier, such deviations could be corrected by improving the LDA with self-energy terms.[39,40]

Qualitative theory-experiment differences are also visible in the FS maps of Fig. 10. The star shape around $\bar{\Gamma}$ is not resolved experimentally, while the size of both the ring structure and the ellipses are slightly larger in the theoretical maps. These shape discrepancies arise from deviations in the theoretical Fermi wave vector values, k_F, which are themselves induced by the energy errors just mentioned above.

However, the most striking property of the experimental FS maps is the threefold symmetry they exhibit, which is at contrast with the 6-fold symmetry of the theoretical FS. This is evident both for the ellipses centered at $\bar{M}$ and for the ring structure; there is a systematic attenuation of the experimental ARUPS yield along the $[\bar{1}21]$ direction compared to the $[1\bar{2}1]$ direction. Anisotropy in the photoemitted intensity has been also reported for the FSs of other surfaces.[44] In explaining this effect, we may rule out the possibility that the electronic structure has a threefold symmetry since, as shown above, all the FS features arise from 2D states; time reversal symmetry adds inversion symmetry to the 2D reciprocal space $[E(k_\parallel)=E(-k_\parallel)]$, so that the corresponding FS will show up as sixfold, as is indeed the case for the theoretical map. The other two, non exclusive, explanations for the broken symmetry in the experimental FS are most probably related either to interference effects in the photoexcitation probability[38] or the actual diffraction process as the photoelectrons emerge from the crystal.

It is also worth mentioning the connection between the electronic structure and the scanning tunneling microscopy (STM) images acquired for the $\mathrm{Si}(111)+p(1\times1)$-$\mathrm{RESi}_2$ systems. It has been suggested in previous works that the atomic scale bright features appearing in the STM images of the RESi_2 surface correspond to Si1 atoms.[7,45,46] Within the Tersoff-Hamann spirit,[47] we have computed the LDOS for the occupied and empty states—integrated over a 0.5-eV energy interval—along a plane parallel to the surface at a normal distance of 2 Å from the Si1. The corresponding plots, shown in Fig. 11, clearly corroborate the assignment of the bright features to the Si1 atoms. However, one should be cautious about this conclusion given the strong approximations involved in this kind of STM simulation.

The atomic structure of all the heavy RE silicides studied until now is analogous. They all stabilize in the B-T4 model depicted in Fig. 1 and only small differences in the atomic layer distances have been reported between them.[12–16] In this work we show that the electronic structures of YSi_2, GdSi_2, and ErSi_2 are coincident too. Their respective ARUPS spectra and FSs can be overimposed without noticeable difference. Therefore, although the theoretical calculations have been exclusively performed for the YSi_2 due to the absence of *f* electrons, we believe that the conclusions derived from our theoretical analysis can be safely generalized for the rest of the heavy RESi_2 presenting the same atomic structure.

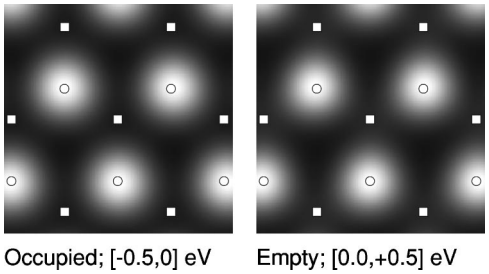

FIG. 11. LDOS plots integrated over the energy ranges indicated at the bottom of each figure, for a plane parallel to the surface and 2 Å above the Si1 atom. The circles (squares) give the location of the Si1 (Si2) atoms.

VI. CONCLUSIONS

The electronic structure and the Fermi surface of the two-dimensional RE silicides epitaxially grown on Si(111) have been studied by a combination of ARUPS and DFT calculations. The two Si atoms at the outermost rotated bilayer bond to each other via a covalent bonding, whereas the RE atom forms an *sp* metallic-type bonding with the neighboring Si atoms together with covalent-type bonds hybridizing the RE *d* states with the Si $3p$ states of the upper and lower Si planes. The nature of the electronic states that shape the FS are found to be surface localized bands, consisting of electron and hole pockets crossing the Fermi energy close to the $\bar{\Gamma}$ and $\bar{M}$ points of the SBZ, respectively. The coincidence between the electronic structure of the Er, Gd, and Y silicides suggests that these bands are inherent to the B-T4 model found more many RE silicides, regardless of the presence or not of *f* electrons.

ACKNOWLEDGMENT

This work has been funded by the Spanish agency 'Dirección General de Investigación' research Project Nos. mat2002-00395 and mat2001-1596 and by Fonds National Suisse pour la Recherche Scientifique. M.E.G. acknowledges financial support by CONACyT and DGAPA-UNAM.

[1] R. Tommes *et al.*, J. Phys.: Condens. Matter **8**, 10231 (1996).
[2] R.D. Thompson, B.Y. Tsaur, and K.N. Tu, Appl. Phys. Lett. **38**, 535 (1981).
[3] K.N. Tu, R.D. Thompson, and B.Y. Tsaur, Appl. Phys. Lett. **38**, 626 (1981).
[4] S. Vandré, C. Preinesberger, W. Busse, and M. Dähne, Appl. Surf. Sci. **78**, 2012 (2001).
[5] L. Magaud, A. Pasturel, G. Kresse, and J. Hafner, Phys. Rev. B **55**, 13479 (1997).
[6] M. Lohmeier, W.J. Huisman, E. Vlieg, A. Nishiyama, C.L. Nicklin, and T.S. Turner, Surf. Sci. **345**, 247 (1996).
[7] C. Polop, C. Rogero, J.L. Sacedón, and J.A. Martín-Gago, Surf. Sci. **482**, 1337 (2001).
[8] M. Lohmeier, W.J. Huisman, E. Vlieg, A. Nishiyama, C.L. Nick-

lin, and T.S. Turner, Phys. Rev. B **54**, 2004 (1996).
[9] M.H. Tuilier, P. Wetzel, C. Pirri, D. Bolmont, and G. Gewinner, Phys. Rev. B **50**, 2333 (1994).
[10] P. Paki, U. Kafader, P. Wetzel, C. Pirri, J.C. Peruchetti, D. Bolmont, and G. Gewinner, Phys. Rev. B **45**, 8490 (1992).
[11] P. Wetzel, C. Pirri, P. Paki, D. Bolmont, and G. Gewinner, Phys. Rev. B **47**, 3677 (1993); P. Wetzel, C. Pirri, D. Bolmont, and G. Gewinner, Appl. Surf. Sci. **65**, 718 (1993).
[12] D.J. Spence, S.P. Tear, T.C.Q Noakes, and P. Bailey, Phys. Rev. B **61**, 5707 (2000).
[13] C. Bonet, D.J. Spence, and S.P. Tear, Surf. Sci. **504**, 183 (2002).
[14] H. Kitayama, S.P. Tear, D.J. Spence, and T. Urano, Surf. Sci. **482**, 1481 (2001).
[15] C. Rogero, C. Polop, L. Magaud, J.L. Sacedón, P.L. de Andrés, and J.A. Martín-Gago, Phys. Rev. B **66**, 235421 (2002).
[16] D.J. Spence, T.C.Q Noakes, P. Bailey, and S.P. Tear, Surf. Sci. **512**, 61 (2002).
[17] D.J. Spence, T.C.Q Noakes, P. Bailey, and S.P. Tear, Phys. Rev. B **62**, 5016 (2000).
[18] L. Stauffer, A. Mharchi, C. Pirri, P. Wetzel, D. Bolmont, G. Gewinner, and C. Minot, Phys. Rev. B **47**, 10 555 (1993).
[19] J. Osterwalder, T. Greber, A. Stuck, and L. Schlapbach, Phys. Rev. B **44**, 13 764 (1991).
[20] D. Naumovic, A. Stuck, T. Greber, J. Osterwalder, and L. Schlapbach, Phys. Rev. B **47**, 7462 (1993).
[21] F. García-Moliner and V.R. Velasco, *Theory of Single and Multiple Interfaces* (World Scientific, Singapore, 1992); M.C. Muñoz, V.R. Velasco, and F. García-Moliner, Prog. Surf. Sci. **26**, 117 (1987).
[22] J. Cerdá, M.A. Van Hove, P. Sautet, and M. Salmerón, Phys. Rev. B **56**, 15 885 (1997).
[23] P. Ordejón, E. Artacho, and J.M. Soler, Phys. Rev. B **53**, 10 441 (1996); J.M. Soler, E. Artacho, J.D. Gale, A. García, J. Junquera, P. Ordejón, and D. Sánchez-Portal, J. Phys.: Condens. Matter **14**, 2745 (2002).
[24] L. Kleinman and D.M. Bylander, Phys. Rev. Lett. **48**, 1425 (1982).
[25] N. Troullier and J.L. Martins, Phys. Rev. B **43**, 1993 (1991).
[26] O.F. Sankey and D.J. Niklewski, Phys. Rev. B **40**, 3979 (1989).
[27] D. Sánchez-Portal, P. Ordejón, E. Artacho, and J.M. Soler (unpublished).
[28] D.M. Ceperley and B.J. Alder, Phys. Rev. Lett. **45**, 566 (1980); J.P. Perdew and A. Zunger, Phys. Rev. B **23**, 5048 (1981).
[29] S. Corbel, J. Cerdá, and P. Sautet, Phys. Rev. B **60**, 1989 (1999).
[30] M. Brandbyge, J.-L. Mozos, P. Ordejón, J. Taylor, and K. Stokbro, Phys. Rev. B **65**, 165401 (2002).
[31] J.B. Pendry, Surf. Sci. **57**, 679 (1976).
[32] C. Meyer, J. Braun, G. Borstel, M. Potthoff, T. Wegner, and W. Nolting, Surf. Sci. **454-456**, 447 (2000).
[33] M. Woods, A. Ernst, P. Strange, and W.M. Temmerman, J. Phys.: Condens. Matter **13**, 8607 (2001).
[34] T. Wegner, M. Potthoff, and W. Nolting, Phys. Rev. B **61**, 1386 (2000).
[35] M. Lindroos and A. Bansil, Phys. Rev. Lett. **75**, 1182 (1995).
[36] W.H. Press, B.P. Flannery, S.A. Teukolsky, and W.T. Vetterling, *Numerical Recipes* (Cambridge University Press, Cambridge, England, 1989).
[37] A.J. Read and R.J. Needs, Phys. Rev. B **44**, 13 071 (1991).
[38] E.L. Shirley, L.J. Terminello, A. Santoni, and F.J. Himpsel, Phys. Rev. B **51**, 13 614 (1995).
[39] O. Pulci, G. Onida, R. Del Sole, and L. Reining, Phys. Rev. Lett. **81**, 5374 (1998).
[40] G.-M. Rignanese, X. Blase, and S.G. Louie, Phys. Rev. Lett. **86**, 2110 (2001).
[41] R.I.G. Uhrberg, G.V. Hansson, J.M. Nicholls, P.E.S. Persson, and S.A. Flodström, Phys. Rev. B **31**, 3805 (1985).
[42] R.J. Hamers, R.M. Tromp, and J.E. Demuth, Phys. Rev. Lett. **56**, 1972 (1986).
[43] J.A. Martín-Gago, J.Y. Veuillen, C. Casado, and T.A. Nguyen Tan, Phys. Rev. B **55**, 5129 (1997).
[44] Th. Pillo, J. Hayoz, H. Berger, F. Lévy, L. Schlapbach, and P. Aebi, Phys. Rev. B **61**, 16 213 (2000).
[45] P. Wetzel, C. Pirri, G. Gewinner, S. Pelletier, P. Roge, F. Palmino, and J.C. Labrune, Phys. Rev. B **56**, 9819 (1997).
[46] J.A. Martín-Gago, J.M. Gómez-Rodríguez, and J.Y. Veuillen, Surf. Sci. **366**, 491 (1996); Phys. Rev. B **55**, 5136 (1997).
[47] J. Tersoff and D.R. Hamann, Phys. Rev. Lett. **50**, 1998 (1983).